Experimental Mechanics
https://doi.org/10.1007/s11340-019-00549-5

RESEARCH PAPER

A Comparative Study of Dynamic Fracture of Soda-Lime Glass Using Photoelasticity, Digital Image Correlation and Digital Gradient Sensing Techniques

S. Dondeti[1] · H.V. Tippur[1]

Received: 1 July 2019 / Accepted: 16 September 2019

Abstract
The dynamic fracture of high-stiffness and low-toughness materials such as soda-lime glass (SLG) typically involves crack initiation and growth prior to branching, underlying mechanics of which is not yet fully understood. Investigation of this issue using full-field optical techniques face numerous spatio-temporal challenges since crack speeds in these materials reach 1500 m/s or more and are accompanied by highly localized deformations. However, often it is tacitly assumed that most optical methods are equally capable of studying this challenging problem and it turns out not to be true. To this end, three prevalent optical techniques - transmission photoelasticity, 2D Digital Image Correlation (DIC) and transmission Digital Gradient Sensing (DGS) - are implemented concurrently to visualize crack-tip fields and quantify fracture characteristics associated with crack initiation, crack growth and macroscopic crack bifurcation in SLG plates subjected to nominally identical loading in three separate experiments. Each method is implemented in conjunction with ultrahigh-speed (1 Mfps) photography, flash/pulse illumination, and a modified-Hopkinson pressure bar for impact loading of specimens. The feasibility of measuring fracture parameters and imposed force histories along with the pros and cons of each approach for this material system are examined.

Keywords Photoelasticity · Digital image correlation · Digital gradient sensing · Dynamic fracture · Transparent glasses and ceramics

Introduction

Transparent glasses and ceramics are routinely used in many civilian and military structures. The dynamic fracture characterization of these high-stiffness and low-toughness materials often pose severe challenges to legacy optical methods because (a) the crack-tip opening displacements and deformations are often extremely small (< 100 nm) and highly localized, (b) the crack growth is highly transient with speeds exceeding 1500 m/s and attained within a couple of microseconds after initiation, and (c) it often involves crack branching. Furthermore, the intriguing phenomenon of self-branching and fracture mode-transition of a dynamically growing mode-I crack to mixed-mode daughter cracks remains unresolved from the mechanics perspective. A range of hypotheses such as the dynamically growing crack-tip (i) reaching a critical velocity, (ii) stress intensity factor attaining a critical value, (iii) hoop stress ahead of it reaching a maximum at an angle other than the self-similar growth direction, (iv) encountering stress wave pile-up ahead of it, (v) provoking microcrack nucleation at increasingly greater distances ahead of it, have all been alluded to as potential causes for crack branching in various theoretical, numerical and experimental reports [1–9]. The absence of an easy-to-use, full-field, optical method capable of mapping deformations over relatively large Regions-of-Interest (ROI) (say, 75 mm × 75 mm) to examine these issues have also been responsible for somewhat limited progress towards addressing these basic questions since popular methods such as photoelasticity, Coherent Gradient Sensing (CGS) and Digital Image Correlation (DIC) are tacitly assumed to be capable of quantifying the mechanical fields near growing cracks in transparent glasses and ceramics. However, it is much more challenging than the perception

Electronic supplementary material The online version of this article (https://doi.org/10.1007/s11340-019-00549-5) contains supplementary material, which is available to authorized users.

✉ H. V. Tippur
tippuhv@auburn.edu

[1] Department of Mechanical Engineering, Auburn University, Auburn, AL 36849, USA

Published online: 13 November 2019

because (a) soda-lime glass (SLG) has a stress-optic constant 30–50 times lower than birefringent polymers often used in photoelastic studies, (b) CGS would need a very large diameter coherent laser beam and an unrealistic grating separation distance (of over 2.5 m when, say, 25 μm pitch Ronchi rulings are used) to laterally shear the object wave front, (c) DIC would need to be able to measure crack-tip displacements of ~100 nm at crack speeds of over 1500 m/s, to name a few. These are indeed severe experimental challenges to the state-of-the-art.

In light of the above, the dynamic fracture mechanics of brittle materials has been studied in the past using loading rate dependent glassy polymers instead. For example, fracture of Homalite-100, a brittle polyester, was used by Dally [10] to visualize a sequence of isochromatic fringes representing the state of stress associated with a crack moving at 200–400 m/s and proposed crack propagation and branching criterion. Bradley and Kobayashi 11] also used edge notched Homalite-100 specimens and a multi-spark gap polariscope cum high-speed camera. They mapped isochromatic fringes associated with the dynamic crack propagation and studied the crack-tip fields surrounding the growing crack experimentally. They characterized the dynamic crack propagation using a two-parameter model. Kobayashi and his associates [12] investigated crack branching via photoelastic experiments, also using Homalite-100 polyester, and proposed a necessary condition based on a critical dynamic stress intensity factor and a sufficient condition of minimum characteristic distance for crack curving. The transmission-mode CGS method was employed by Tippur et al. [13] and Krishnaswamy et al. [14] to investigate dynamic crack growth in edge-cracked PMMA plates subjected to impact loading by mapping crack-tip stress gradients near growing cracks.

The optical methods have also played a significant role in studying dynamic fracture mechanics of non-transparent brittle materials. A reflection-mode CGS was introduced by Tippur et al. [15] to study front-coated PMMA mirrors and subsequently to evaluate notch initiation toughness of bulk metallic glasses [16]. Lately, DIC methods have been popular in the study of dynamic fracture mechanics of polymers, metals, and composites as they are relatively easy-to-implement and provide full-field displacement information. Kirugulige and Tippur [17] were the first to characterize dynamic fracture of epoxy-based syntactic foams using 2D DIC and ultrahigh-speed multi-sensor digital photography. They mapped crack opening and sliding displacements around a moving crack-tip and quantified temporal evolution of fracture parameters. Lee and Tippur [18] extended DIC to investigate stress-wave induced fracture of graphite fiber reinforced epoxy laminates. The instantaneous crack-tip locations were identified using high-speed photographs to determine dynamic crack growth behavior in terms of stress intensity factors and energy release rate histories to study fiber orientation effects. Feiteira et al. [19] studied brittle fracture due to excessive strain in polymer-based self-healing concrete using DIC and reported that failure due to brittle fracture of a rigid foam was detected at around 9% strain. Makki et al. [20] investigated laminated glass due to blast loading using 3D DIC to evaluate structural integrity. They observed that both interlayer and coating materials survived the shock loading without catastrophic failure despite substantial fragmentation. Reu et al. [21] proposed a method for measuring crack lengths by determining full-field surface strains during sub-surface crack growth in aluminum specimens using DIC along with x-rays.

In addition to the above popular optical methods applied to investigate fracture, a full-field optical method called Digital Gradient Sensing (DGS) to measure small angular deflections of light rays proportional to in-plane stress gradients in transparent solids was introduced recently by Periasamy and Tippur [22]. The authors demonstrated the utility of the method for both static and dynamic investigations [23]. Recently, Sundaram and Tippur [24] extended DGS to study dynamic crack-interface interactions in PMMA bilayers. They observed different crack growth behaviors across a discrete interface perpendicular to the incoming mode-I crack. The measured crack-tip parameters showed that if the interface experienced tensile stress waves in excess of its tensile strength, a debond nucleation occurred at the interface prior to the arrival of the mode-I mother crack resulting in branching; otherwise branching did not occur [25]. More recently, Sundaram and Tippur [26, 27] have used DGS coupled with ultrahigh-speed photography to characterize static and dynamic fracture of SLG. They were able to quantify fracture parameters including crack velocity, stress intensity factors, and energy release rate from their optical measurements at crack initiation and at crack branching.

In the following, three different full-field optical methods are comparatively examined to study dynamic fracture of SLG under nominally identical conditions but in separate experiments. Experimental setups and procedures adopted for each method are described and the resulting measurements are presented and analyzed to the extent feasible. Based on the outcomes, the pros and cons of each method for studying this challenging material system are noted.

Specimen

Commercially procured transparent SLG plates were used to study dynamic mode-I crack growth leading to branching. Specimens were cut using a resin-bonded diamond blade from a single large 5.7 mm thick SLG plate into samples of 150 mm length, and 100 mm width. A symmetric 40° V-notch was introduced at the mid-span of the specimen along the long edge, as shown in Fig. 1. The apex of the notch-tip was further extended by 8 mm with a diamond impregnated circular saw

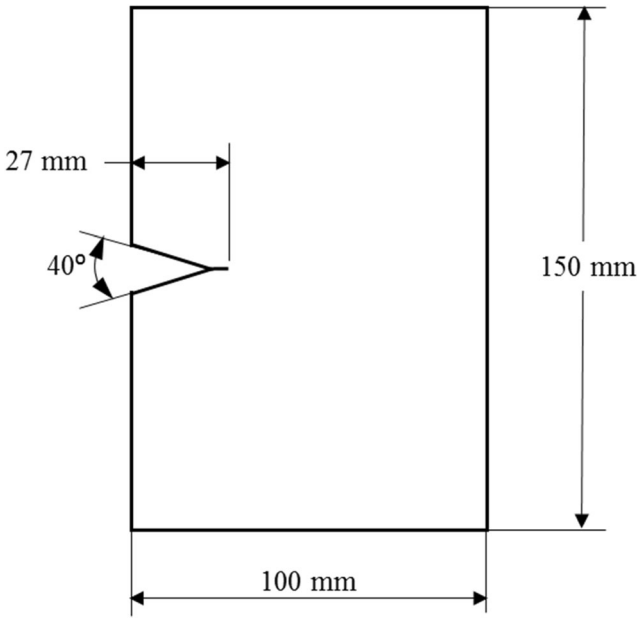

Fig. 1 V-notched soda-lime glass specimen with an extended notch. (Thickness = 5.7 mm)

of 0.3 mm thickness. A few relevant mechanical and physical properties of SLG are listed in Table 1.

Photoelastic Study

Experimental Details

Photoelasticity is one of the well-established full-field optical methods which can be used to study dynamic fracture of birefringent materials. In the past, it has been extensively used to investigate dynamic fracture behavior of glassy polymers such as epoxies, polycarbonate, and polyesters [10, 11]. SLG being a birefringent material, an attempt to investigate crack initiation leading to branching using this popular method was considered first. An incoherent, monochromatic, LED pulse light source was used for illuminating the specimen in a standard dark field circular polariscope. An ultrahigh-speed digital camera (Kirana model 05 M from Specialized Imaging, Inc.) was used to capture the emergent light waves exiting the analyzer as interference fringes proportional to the local principal stress differences.

Table 1 Some relevant soda-lime glass properties

Property	Value
Density, ρ	2500 kg/m^3
Longitudinal wave speed, C_L	5700 m/s
Shear wave speed, C_S	3400 m/s
Rayleigh wave speed, C_R	3100 m/s
Elastic modulus, E	70 GPa
Poisson's ratio, υ	0.22
Tensile strength, σ_t	41–180 MPa
Compressive strength, σ_c	330 MPa
Elasto-optic constant, C_σ	-0.027×10^{-10} m^2/N
Stress-optic constant, f_σ	0.22 MPa-m/fringe

The dynamic fracture experiments on SLG specimens were performed using a setup shown schematically in Fig. 2. The stress wave loading of the specimen leading to crack initiation, crack growth, and failure mode transition involving crack branching were all recorded during the experiment. A modified Hopkinson pressure bar (1830 mm long and 25.4 mm diameter C-300 maraging steel rod) with a symmetrically tapered blunt tip matching the V-notch was used to impact an unconstrained ('free-free') specimen. Approximate free support conditions were created for the specimen by placing it on a ~4 mm thick strip of soft-putty laid down on a height-adjustable translation stage. The opposite edge of the specimen was also pressed-on with an identical putty strip to create symmetry in terms of acoustic impedance relative to the loading axis. Other edges, with the exception of the V-notch flanks, were free as well. A 305 mm long, 25.4 mm diameter cylindrical steel striker, held inside a gas-gun barrel and aligned co-axially with the long-bar was used to subject the sample to stress wave loading. Once the striker was launched by the gas-gun, the collision between the striker and the long-bar (impact velocity ~6 m/s) generated a stress pulse which subsequently loaded the upper and lower flanks of the V-notch after propagating along the long-bar. When the striker contacted the long-bar, a trigger pulse was generated by a DC circuit to initiate recording of images by the camera which in turn triggered the laser unit (SI model LUX640) to emit synchronized laser pulses. The illumination source produced a string of 160 ns duration pulses in sync with the camera exposure to capture the photoelastic fringes. An adjustable delay generator was used in series with the trigger pulse unit and the camera, to account for the time lapse assocated with the stress wave propagation along the length of the long-bar before the specimen was loaded. In these experiments, 320 μs delay was used. The single sensor ultrahigh-speed camera with 924 × 768 pixels spatial resolution (10-bit gray scale images) was operated at 1 million frames per second to record 180 full resolution images. The camera was located at a distance of approx. 3.86 m in front of the specimen. A Nikkor 400 mm focal length f/2.8 macro lens along with a Nikon focal length doubler (or 2X tele-converter) and adjustable bellows (Nikon PB6) were used. An aperture setting of $F^{\#}16$ was necessary to achieve good focus and satisfactory exposure. The ROI in this study was such that contact stress evolution, crack initiation, crack propagation, and branching could all be observed successively in a single experiment. Based on a few trials, photographing a rectangular region of 85 × 74 mm^2 on

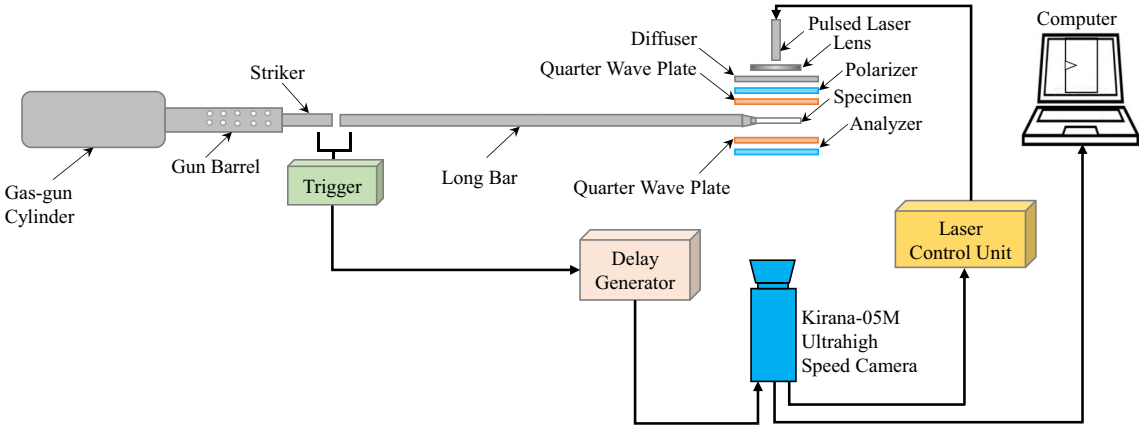

Fig. 2 The schematic of experimental setup (top-view) for photoelasticity with dark-field circular polariscope

the specimen plane was found necessary to achieve this requirement.

Crack Length, Velocity

The evolution of photoelastic fringes, proportional to principal stress difference, from the instant the loading on the crack flanks begins to mother crack initiation at the notch-tip, its subsequent growth as a mode-I crack, mode transition to two dominant mixed-mode daughter cracks was recorded. (A video animation of the same for visualization purposes is available as supplementary material.) Upon impact, a mode-I crack first initiated and then propagated approximately to the middle of the specimen width (~24 mm from the original notch-tip), then branched into two macroscopic mixed-mode (mode-I + mode-II) daughter cracks[1] globally symmetric relative to the loading axis, as evident from the reassembled fractured specimen shown in Fig. 3. A few select instantaneous fringes from the optical history are shown in Fig. 4(a)-(d). Figures 4(a) and (b) correspond to mode-I crack initiation and growth, respectively, whereas Figs. 4(c) and (d) correspond to fracture mode-transition in the early and late stages resulting in two mixed-mode daughter cracks. (For illustration purposes, the brightness of some of these images is enhanced, and therefore the intensity field outside the specimen appears slightly lighter than the original recordings.)

A few qualitative observations can be made from Fig. 4. As evident from the individual images (and the video in the supplementary material), the crack-tip locations at each time instant is rather clear during the entire fracture event. Additionally, two groups of fully-formed fringe lobes immediately adjacent to the two crack flanks represent contours of principal stress differences due to two equal and opposite compressive forces imposed on the specimen during stress wave loading. Under the assumption of negligible friction, these contours could be analyzed to estimate the instantaneous force magnitudes using the optical fringes in conjunction with an available closed-form solution. However, *since the crack-tip vicinity is subjected to tensile stresses, it does not show fully-formed fringes required for quantitative analysis*. Hence, extracting the crack-tip stress intensity factors, as reported previously with glassy polymers [10], is not feasible here. This stark difference regarding the availability of well-formed macrosize fringes at the impact locations and crack-tip is attributed to the low tensile failure strain of SLG relative to its compressive counterpart. That is, SLG can support significantly higher compressive stresses when compared to the tensile counterparts. Additionally, it can be observed in Fig. 4 that the propagating crack is trailed by gangs/groups of tiny fringes resembling stitch-marks along the crack path. They are attributed to Rayleigh waves propagating along the two crack flanks causing periodic contact between the deformed upper and lower lips as the crack opening displacements are in the sub-micron scale. The spatial interval between these gangs of

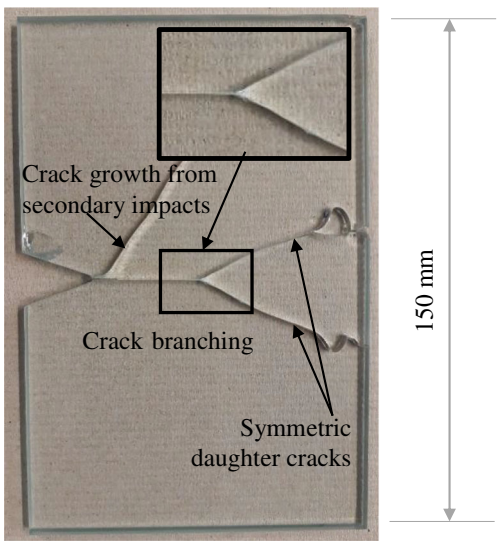

Fig. 3 Reconstructed fractured specimen used in photoelasticity experiment

[1] A hint of an unsuccessful mode-I self-similar crack growth along its original path is evident in the fractured sample though it is not evident in the interferograms.

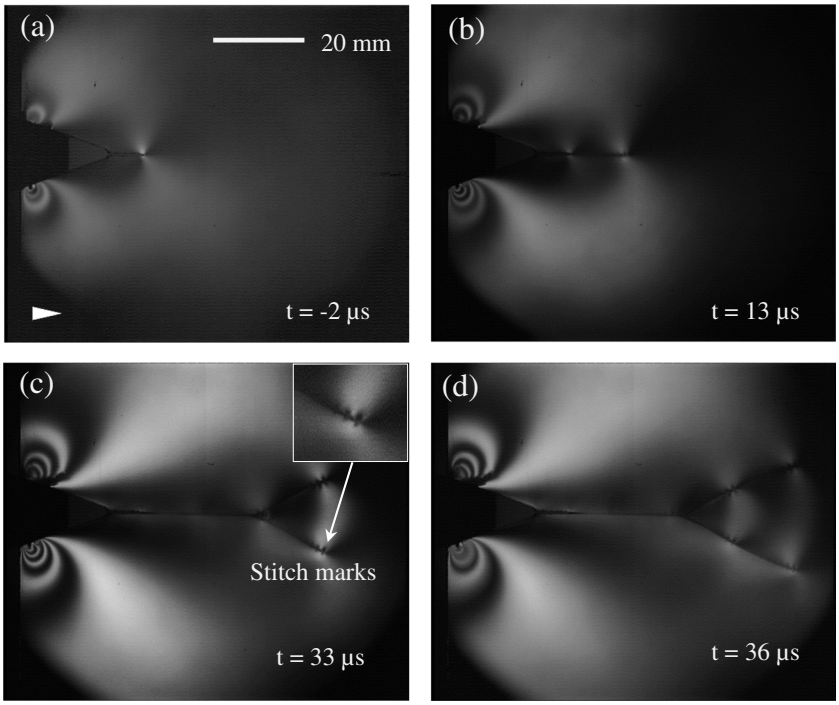

Fig. 4 Photoelastic fringes in soda-lime glass specimen subjected to dynamic loading. Arrowhead (in the top left image) represents crack growth direction. Time, $t = 0$ corresponds to crack initiation at the original notch-tip. The 'stitch marks' along the crack path are attributed to contact stresses due to the Rayleigh waves

fringes was estimated from the images resulting in a speed of 2900 ± 100 m/s, which is close to the Rayleigh wave speed for SLG (Table 1).

Although well-formed crack-tip fringes required for extracting fracture parameters were absent near the growing crack, the spatial position of the crack-tip could be easily detected from the photographed images to obtain crack length history accurately during the entire fracture event. The uncertainty of locating the crack-tip was less than 0.2 mm. This could affect the computed crack velocities evaluated via numerical differentiation. To minimize errors in the instantaneous crack speed, a quadratic Bézier curve [24, 28] was fitted to the crack length data at a time instant 'i' as,

$$a_i(s) = (1-s)^2\hat{a}_i + 2s(1-s)\hat{a}_{i+1} + s^2\hat{a}_{i+2}, 0 \le s \le 1 \qquad (1)$$

where s, $\hat{a}$ and a are smoothing parameter, measured crack length, and the smoothed crack length, respectively. In the above expression $\hat{a}_i, \hat{a}_{i+1}, \hat{a}_{i+2}$ are the control points of $a_i(s)$. The value of s was chosen as 0.5 such that the smoothed data point was at the middle of each interval. Subsequently, the crack velocity (V) was estimated from the smoothed crack length history using backward difference approximation,

$$V_i = \frac{a_i - a_{i-1}}{t_i - t_{i-1}} \qquad (2)$$

where a and t are crack length and time, respectively. Figures 5(a) and (b) represent the apparent crack length and velocity histories, respectively. Here $t = 0$ corresponds to crack initiation at the original notch-tip. The crack length increased monotonically from initiation to the end of the observation

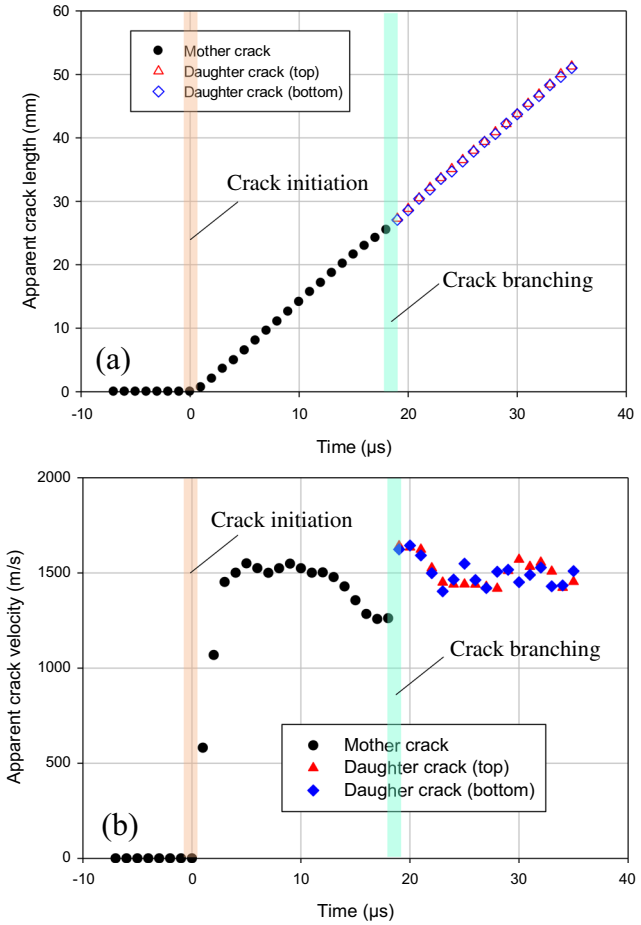

Fig. 5 Apparent crack length (top) and crack velocity (bottom) histories from photoelasticity. (Time, $t = 0$ corresponds to crack initiation at the original notch-tip)

window, including branching. A small change in the slope is noticeable before and after the crack branching event that occurred over 16–19 μs after crack initiation. The measured crack-tip locations from the two mixed-mode daughter cracks were such that the crack length data essentially overlapped on each other with an excellent symmetry in the overall branching phenomenon observed during this experiment. The crack velocity of the mode-I crack increased steadily to ~1400 m/s rapidly, within the first 2–3 μs after initiation, before attaining a *nearly constant velocity* in the 1400–1600 m/s range until ~12 μs after crack initiation. Furthermore, prior to the mode-I crack entering the branching phase, the *apparent* crack velocity gradually decreased to ~1250 m/s. Subsequently, the propagating mode-I crack branched to produce two globally symmetric mixed-mode daughter cracks which almost instantaneously (within 1–2 frames) reached ~1600 m/s before settling back to steady values over the next 4 μs. The daughter crack velocities were again in the range of 1400–1600 m/s, same as the steady-state values of the mother crack. These trends are similar to the one observed in [27], and the drop in crack velocities prior to branching are attributed to the increasing surface roughness in the so-called 'hackle' phase [2] of crack growth. Similary, the rapid increase in crack velocities after branching punctuate the daughter cracks entering (or returning to) the so-called 'mirror' phase [27] and a steady crack velocity of ~155 m/s.

Impact Force History

The force histories on the V-notch faces of the specimen by the long-bar were evaluated from the photoelastic fringes. The shape of the fringe lobes suggests approximate line-loading of each of the two flanks of the V-notch. Accordingly, for ease of interpretation, each interferogram was used in conjunction with the Flamant's solution for line-load acting normally on the edge of a planar elastic solid. Using the closed-form solution [29] along with the stress-optic law, the normal force on the specimen flanks were estimated using,

$$\frac{Nf_\sigma}{B} \approx \frac{2F(t)}{\pi r B} \tag{3}$$

where N is fringe order, f_σ is the stress-optic constant (= 220 N/m/fringe for SLG), r is the radial distance of the fringes measured from the contact point (origin) and B is the specimen thickness. Both the dark and light fringes were analyzed by assigning integer and half orders, respectively. The contact force was evaluated at each of the fringe locations and averaged at each time instant ($t = 0$ corresponds to mode-I crack initiation event at the notch-tip). The resulting normal force history is shown in Fig. 6. The histories for the upper and lower flanks were computed separately (blue and red symbols) and averaged (solid line). Apart from the expected

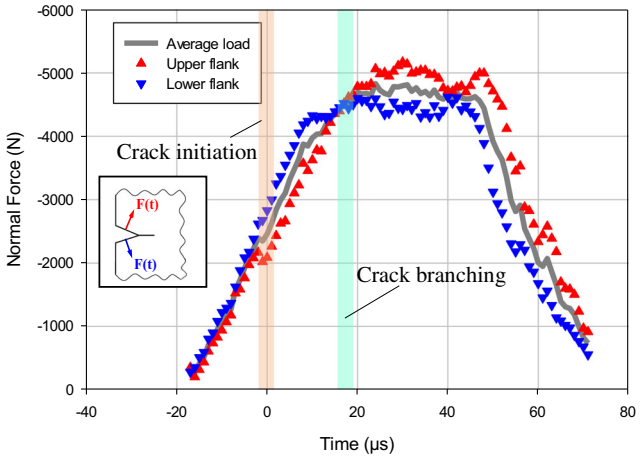

Fig. 6 Contact force history from photoelasticity (Time, $t = 0$ corresponds to crack initiation at the original notch-tip)

measurement differences, the force histories of the two flanks follow approximately 'ramp-up, plateau, ramp-down' pattern. An estimated loading rate during the ramp-up phase is of approx. 150 MN/s. The overall loading period the analysis could be performed satisfactorily was about 100 μs. A peak load of 4800 ± 150 N in the plateau region was realized during the dynamic loading event.

Digital Image Correlation (DIC)

Experimental Details

Currently, the digital image correlation methods are popular for full-field experimental mechanics studies, including dynamic fracture mechanics investigations [17, 30–35]. Previous works have utilized DIC to study many traditional metallic and polymeric materials. To date, however, there are no reports on examining the feasibility of DIC to quantitatively study *rapidly growing* cracks in glasses and ceramics subjected to stress wave loading. Yet, it is generally presumed that the method would work. Accordingly, an attempt to examine crack initiation, growth and branching phenomena in SLG specimens of geometry and loading configuration described in the previous section was undertaken. That is, the V-notched specimen (Fig. 1) was spray painted with uniform but random black/white speckles pattern. The ROI on the specimen for imaging purposes was maintained same as in the one in the photoelastic study (85 × 74 mm^2) in order to capture all the three fracture events, crack initiation - growth - branching, in a single specimen. (It should be noted here that, 2D DIC being scale independent method, nanoscale speckles created over sub-mm or a couple of mm size ROI would not be practical for capturing all the intended phases of fracture behavior targeted in this work.) The specimens were subjected to impact loading using the experimental setup shown schematically in Fig. 7. It is similar to the one shown in Fig. 2

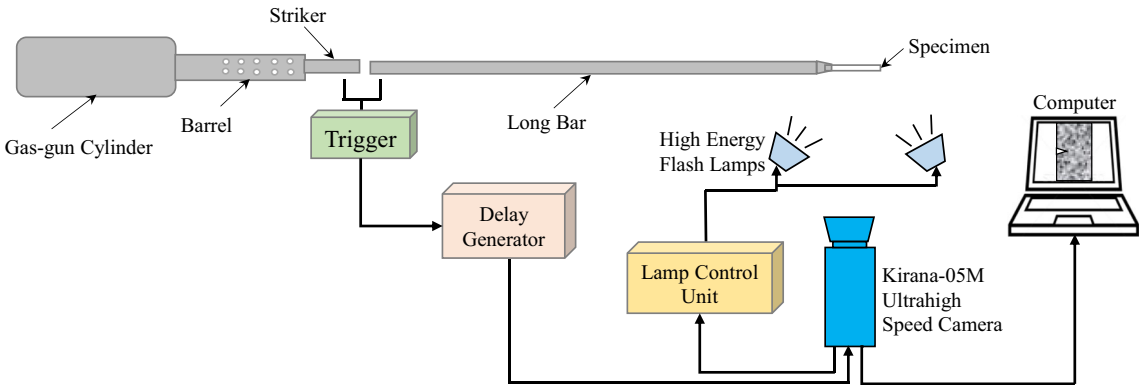

Fig. 7 Schematic of experimental setup (top-view) for DIC to study dynamic fracture of soda-lime glass

but was modified for recording the random speckles directly off the specimen surface. That is, the speckle images were captured in the undeformed/reference and deformed states of the specimen using the same ultrahigh-speed camera, Kirana-05 M, operating at the same framing rate of 1 Mfps, as in the photoelasticity experiment. The specimen was illuminated by two broad-spectrum xenon flash lamps. Again, a Nikon 400 mm/F2.8 lens along with a focal length doubler and an adjustable bellows was used to achieve good focus from a distance of 3.86 m from the specimen plane. The lens aperture was stopped-down to $F^{\#}16$ after focusing on the speckles to increase the depth-of-focus. The corresponding angle-of-view was approx. 1.3 deg.

Two speckle images from the post-impact regime ($t = 0$ again corresponds to crack initiation at the initial notch-tip) are shown in Fig. 8, where the direction of crack growth is indicated by the arrowhead. Despite an excellent quality of the recorded speckles images, unlike in the photoelastic counterparts (Fig. 4), neither the growing hair-line crack nor the instantaneous crack-tip is discernible even after close examination. Accordingly, a *probable* region where the crack-tip resides at that time instant is highlighted by a dotted circle in these images. Subsequently, using principles of DIC, sub-images in the reference state were located in various deformed images via gray scale correlation operation [36] using image analysis software ARAMIS® (GOM mbH, Braunschwelg, Germany). This involved segmenting the speckle images into 30 × 30 pixel sub-images with an overlap of 5 pixels between neighboring sub-images. Once the location of the corresponding sub-image in the deformed state was identified, the local displacements were quantified at the center of each sub-image. This resulted in u and v displacement data arrays, each of 147 × 178 size in the ROI corresponding to horizontal and vertical directions, respectively. It should be noted that the larger sub-image sizes of 40 × 40 and 50 × 50 pixels were tried and they did not improve our ability to locate the crack-tip as the displacements are expected to be in the sub-micron level.[2]

As in the photoelastic experiment, the crack initiated at the original notch-tip and propagated under dominant mode-I conditions for a distance of ~25 mm before bifurcating into two globally symmetric mixed-mode daughter cracks. The dynamic crack initiation event produced a hairline crack from the pre-notch-tip but, as noted earlier, could not be discerned directly from the speckle images (see, Fig. 8). Accordingly, the in-plane displacement fields were plotted from the u and v

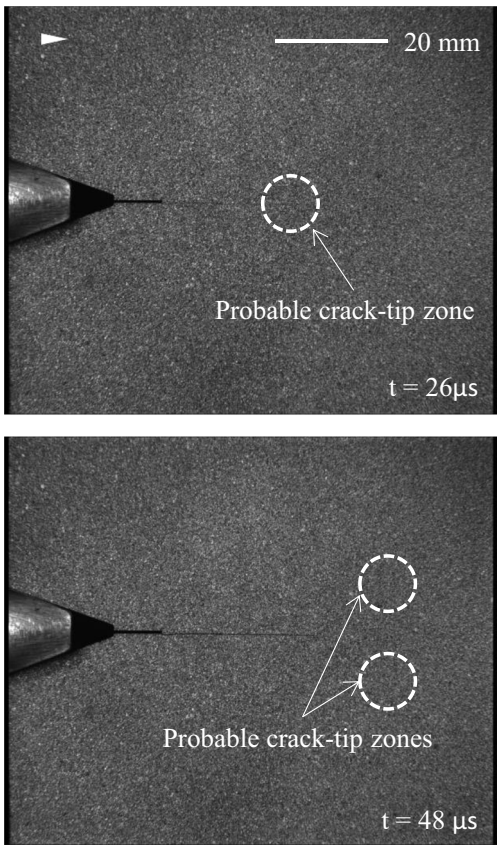

Fig. 8 DIC speckle images subjected to dynamic loading. Arrowhead represents crack growth direction. (Time, $t = 0$ corresponds to crack initiation at the original notch-tip)

[2] It should also be noted that an additional image analysis software Vic-2D with and without 'fill-boundary' option [37] was also used and the results were similar to those from ARAMIS. Details are suppressed here for brevity.

data arrays as contours in the ROI. The expected jump in the *v*-displacements across the crack flanks behind the crack-tip and convergence of *v*-displacement contours were considered to locate the instantaneous crack-tip at each time step [26]. It should be noted that the strain component fields were also plotted (not shown) and were very noisy despite using different sub-image sizes while performing speckle correlation.

Crack Length, Velocity

The dominant *v*-displacement (in the vertical direction with respect to mode-I propagating mother crack) obtained from image correlation were plotted for all time instants. Video animations of contours of this field during the fracture event are included as supplementary material. A few select images, before and after crack branching, are shown in Fig. 9. The lowest possible contour increment of 2 μm was used for plotting displacement fields based on 2% of the pixel size, close to the limit of DIC method's capability. It should be noted that since displacements are non-singular, locating the crack-tip precisely when compared to photoelasticity was indeed a challenge. It is worth pointing out that, to tackle this issue, methods such as nonlinear least-squares regression with crack-tip position as an unknown, genetic algorithms, subset splitting, to name a few, have all been proposed. These approaches, however, are computationally expensive due to additional variables; more importantly, numerical convergence nor accuracy is not assured even for traditional polymers and metal substrates [31], [38–40] where displacements are two orders of magnitude higher than SLG. Furthermore, the feasibility of these methods when crack flank displacements are in the sub-micron scale is unknown and hence was not pursued in this work.

From the probable crack-tip locations thus identified, the *apparent* crack length histories were evaluated from displacement field maps, see Fig. 10(a). As in the photoelastic experiment, the crack length increased with the passage of time (again $t = 0$ corresponds to crack initiation at the original tip) until crack branching (between 16 and 17 μs) and beyond. The crack length history is rather noisy when compared to the one from the photoelastic experiment (Fig. 5), with frequent and unexplainable crack length *reductions* at some of the time instants relative to the previous step/s. The crack growth also seems to have stalled before crack branching, inconsistent with Fig. 11. In addition, the two daughter crack lengths did not match temporally with each

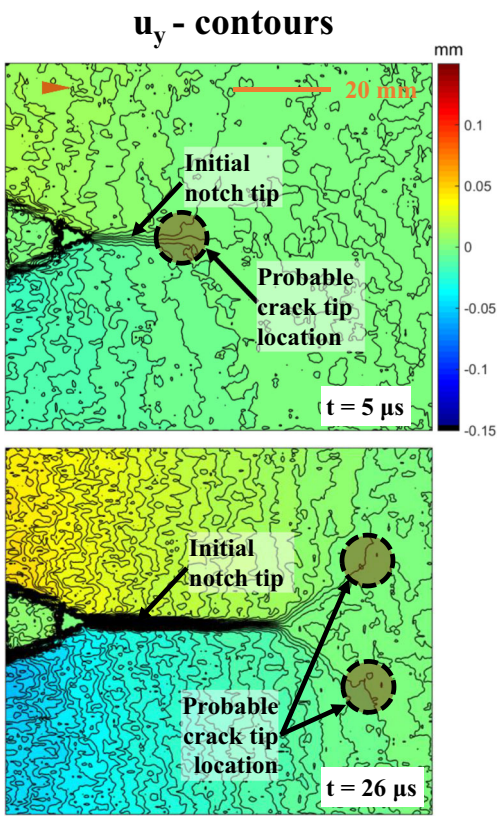

Fig. 9 Displacement contours on soda-lime glass specimen surface along the vertical direction (normal to the mode-I crack propagation) from DIC at ~5 μs and ~26 μs after crack initiation at the original notch-tip

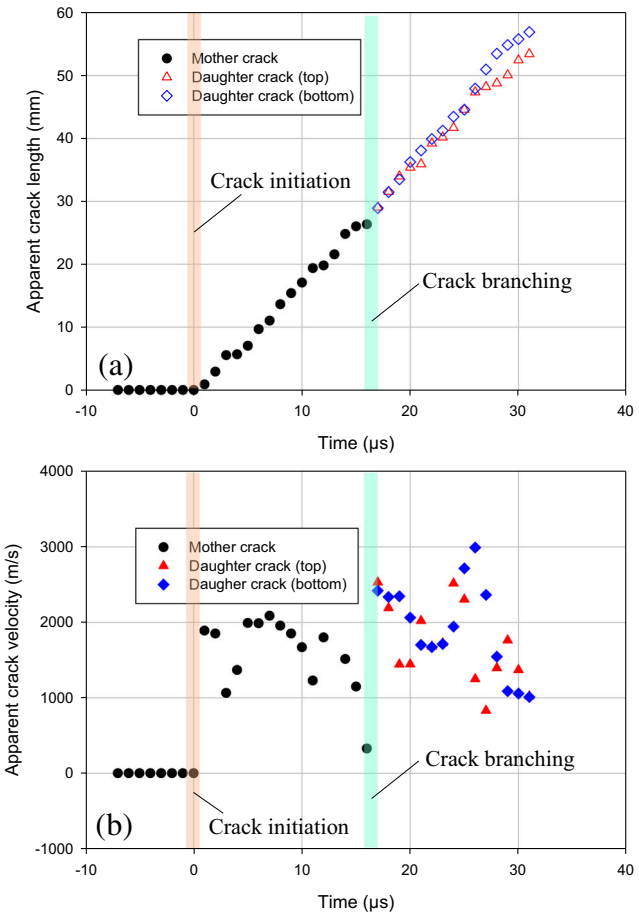

Fig. 10 Apparent crack length (top) and velocity (bottom) histories from DIC. (Time, $t = 0$ corresponds to crack initiation at the original notch-tip)

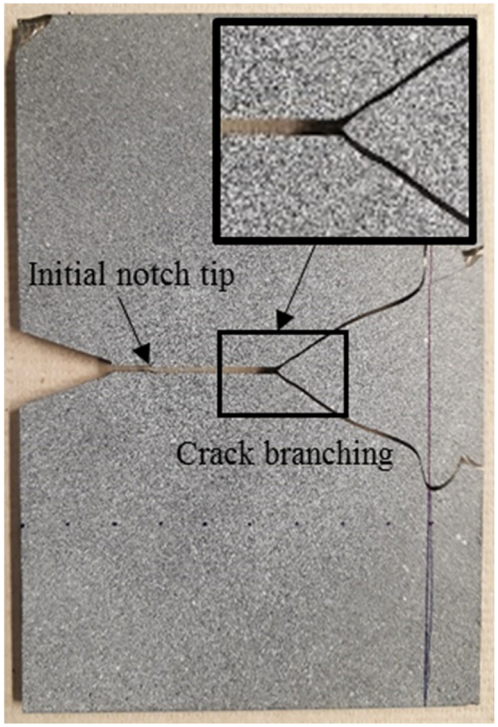

Fig. 11 Reconstructed fractured specimen used in DIC experiment

other even though the branching was exceptionally symmetric based on the reassembled specimen shown. These anomalies were attributed to large uncertainties in finding the moving crack-tip location from DIC. By overlooking these anomalies in the crack length history, the data was smoothed (Eq. 1 and 2) and crack velocities were determined using backward difference approx. and are as shown in Fig. 10(b). The outcome was that the crack velocity increased to 1890 m/s instantaneously and fluctuated over a relatively wide range, from 1060 m/s to 2370 m/s, until the crack branched. After branching, the velocity increased instantaneously to an unrealistic ~2400 m/s which subsequently was in the range of 800–3000 m/s for ~11 μs. Due to high-stiffness and low-toughness of SLG, crack flank displacements near the crack-tip are expected to be extremely small, estimated to be ~80 nm. Therefore it was concluded that finding the crack-tip location using convergent displacement contours was not just challenging, but resulted in very noisy and unreliable crack velocities in SLG.

Stress Intensity Factors

Despite the challenges of locating the crack-tip from the displacement field measurements, for completeness the mode-I stress intensity factors were evaluated from the data around the crack-tip in conjunction with the elasto-dynamic asymptotic equations [17] and over-deterministic least-squares analysis. For a dynamically propagating crack, the crack opening displacements are given by,

$$u_y = \sum_{n=1}^{N} \frac{\left(K_I^d\right)_n B_I(c)}{2\mu}\sqrt{\frac{2}{\pi}}(n+1)\left\{-\beta_1 r_1^{\frac{n}{2}} \sin\frac{n}{2}\theta_1 + \frac{h(n)}{\beta_2} r_2^{\frac{n}{2}} \sin\frac{n}{2}\theta_2\right\} + \sum_{n=1}^{N} \frac{\left(K_{II}^d\right)_n B_{II}(c)}{2\mu}\sqrt{\frac{2}{\pi}}(n+1)\left\{\beta_1 r_1^{\frac{n}{2}} \cos\frac{n}{2}\theta_1 + \frac{h(\overline{n})}{\beta_2} r_2^{\frac{n}{2}} \cos\frac{n}{2}\theta_2\right\}, \quad (4)$$

(where) $r_m = \sqrt{x^2 + \beta_m y^2}, \theta_m = \tan^{-1}\left(\frac{\beta_m y}{x}\right), m = 1, 2$

$$\beta_1 = \sqrt{1-\left(\frac{c}{C_L}\right)^2}, \beta_2 = \sqrt{1-\left(\frac{c}{C_S}\right)^2}$$

$$C_L = \sqrt{\frac{(\kappa+1)\mu}{(\kappa-1)\rho}},\ C_S = \sqrt{\frac{\mu}{\rho}},\ \kappa = \frac{3-\nu}{1+\nu} \text{ for plane stress}$$

$$h(n) = \begin{cases} \frac{2\beta_1\beta_2}{1+\beta_2^2} \text{ for odd } n \\ \frac{1+\beta_2^2}{2} \text{ for even } n \end{cases}$$

and $h(n) = h(n+1)$

$$B_I(c) = \frac{\left(1+\beta_2^2\right)}{D},\ B_{II}(c) = \frac{2\beta_2}{D}, D = 4\beta_1\beta_2 - \left(1+\beta_2^2\right)^2.$$

In the above, (x, y) and (r, θ) are the Cartesian and polar coordinates instantaneously aligned with the current crack-tip, respectively, c is crack velocity, C_L and C_S are longitudinal and shear wave speeds of the material, μ is shear modulus and υ is Poisson's ratio. Again $(K_I)_{n=1}$ and $(K_{II})_{n=1}$ are the mode-I and mode-II dynamic SIF, respectively. Figure 12 shows SIFs evaluated from the data around the crack-tip in the region $0.5 \le (r/B) \le 1.5$ with an angular extent of $-150° \le \theta \le 150°$ [38] and over-deterministic least-squares analyses. Similar to the velocity plot, the SIF data are extremely noisy due to an

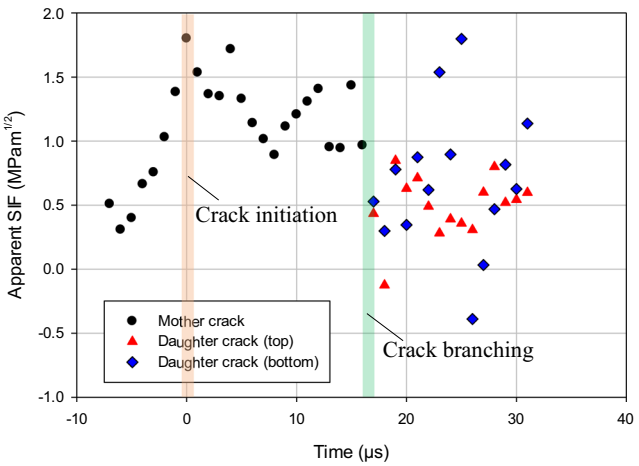

Fig. 12 Apparent mode-I stress intensity factor histories extracted from DIC. (Time, $t = 0$ corresponds to crack initiation at the original notch-tip)

inaccurate crack-tip location compounded by large errors in crack velocity. The mode-I SIF values increased to ~1.8 ± 0.4 MPa√m until crack initiation before dropping due to the local unloading upon crack initiation. After crack branching, mode-I SIFs varied randomly without following a reasonable trend until the end of the observation window. The mode-II SIFs evaluated simultaneously are not included here simply due to the difficulty in comprehending very large errors.

Digital Gradient Sensing (DGS) Method

Experimental Details

A third, relatively new method, Digital Gradient Sensing or DGS, was used next to visualize and quantify crack initiation, growth and branching phenomena and comparatively evaluate the measurements with the previous two methods. Briefly, in *this technique which utilizes DIC*, the random speckle pattern is on a planar 'target' and *not* on the transparent specimen and, it is photographed through the specimen being studied. The gray scales on the target are illuminated using ordinary polychromatic light. To obtain a reference image, the speckle pattern on the target is photographed first in the undeformed/reference state of specimen. That is, the camera captures gray scale information at point P on the target plane (x_0-y_0 plane) through a point O on the specimen plane (x-y plane). Upon loading, the non-uniform state-of-stress produces changes in refractive index of the specimen in the crack-tip vicinity. In addition, the Poisson effect alters the thickness non-uniformly. A combination of these two phenomena referred to as the *elasto-optic effect*, deflect light rays from their original path as they propagate through the stressed specimen. The speckle pattern is once again photographed through the specimen in the deformed state. After deformation, the camera records a neighboring point Q on the target plane through the same point O on the specimen plane. By correlating deformed and reference speckle images, local shifts in speckle clusters, δ_x and δ_y, can be quantified using image correlation algorithms. By knowing the distance between the specimen plane and the target plane, the angular deflections of the light rays ϕ_x and ϕ_y in two orthogonal planes (x-z and y-z planes, the z-axis coinciding with the optical axis of the setup and x-y being the specimen plane coordinates) can be evaluated. These angular deflections have been previously shown to be proportional to the gradients of the in-plane normal stresses as,

$$\phi_{x;y} = \pm C_\sigma B \frac{\partial(\sigma_x + \sigma_y)}{\partial x; y} \tag{5}$$

where C_σ is the elasto-optic constant of the material, B is its initial thickness, $(\sigma_x + \sigma_y)$ is the first stress invariant under plane stress condition, and σ_x and σ_y denote the thickness-wise averages of Cauchy's normal stress components.

A schematic representation of the experimental setup for transmission-mode DGS [22] technique is shown in Fig. 13. As in the photoelasticity and DIC counterparts, experiments were performed using a modified Hopkinson pressure bar or a long-bar impactor, see Fig. 14. Again, the crack initiation, growth and branching were recorded using ultrahigh-speed photography for a loading pulse duration of ~120 μs. When the striker impacted the long-bar, a trigger pulse was generated to initiate the camera and capture speckle images off the target plane through the specimen. Simultaneously, the high-speed camera triggered a pair of xenon high-energy flash lamps. A delay generator was also used in the trigger circuit as the stress wave had to propagate along length of the long-bar before loading the specimen. In these experiments, a delay of 320 μs was used. Again, a Kirana-05 M ultrahigh-speed digital camera operating at 1 million frames per second with 924 × 768 pixels spatial resolution (10-bit gray scale images) recorded 180 full resolution images. The camera was situated at a distance of 3.86 m in front of the specimen, whereas the speckle target was at a distance of 1.0 m behind specimen. A Nikkor 400 mm focal length, F#2.8 lens along with a focal length doubler and adjustable bellows were used to record speckles on the target plate. After focusing on the speckles, the aperture was reduced to $F^{\#}16$ to enhance depth of focus and a good exposure. A 110 × 92 mm^2 region on the target corresponding to approx. 88 × 65 mm^2 ROI on the specimen (based on pin-hole approx.) was photographed. Besides monitoring the contact stresses on the crack flanks, the ROI covered crack initiation, propagation and branching events, all in a single experiment.

Crack Length, Velocity

Two representative speckle images recorded, one in the undeformed/reference and the other in the deformed states of specimen is shown in Fig. 15. These speckle images are provided for completeness even though they are not visually informative. That is, the speckles or deformations around the crack-tip are not readily visible except a blob of distorted speckles in the deformed specklegram when observed carefully relative to the undeformed counterpart. This is because the camera focused on the target instead of the specimen. However, the resulting angular deflections of light rays and hence deformations become apparent after correlating the images. A photograph of the fractured specimen from this experiment is shown in Fig. 16. After initiation at the original notch-tip, the crack propagated as a mode-I mother crack and subsequently branched into two mixed-mode daughter cracks at approx. 26 mm from the initial tip. The branched cracks maintained global symmetry relative to the mother crack as shown in Fig. 16. Finally, when the two daughter cracks approached the specimen edge, the crack paths were visibly disturbed due to the loss of in-plane constraint.

The angular deflection contours for $\phi_x$and ϕ_y in two orthogonal directions (with respect to mode-I propagating mother crack)

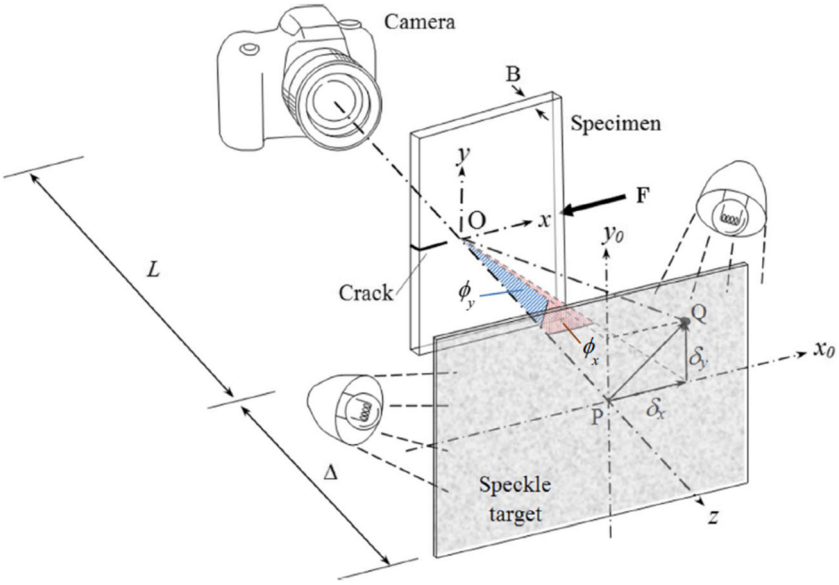

Fig. 13 The schematic representation of Digital Gradient sensing (DGS) technique to determine planar stress gradients [23]

along with the resultant values of angular deflections $\phi_r \left(= \sqrt{\phi_x^2 + \phi_y^2}\right)$ at select time instants are shown in Fig. 17 as contours even though the data are available as rectangular arrays. A video animation encompassing the evolution of contact stress induced deformation of the V-notch flanks, crack initiation, growth and branching events is available in the supplementary materials section. The $\phi_x$contours are symmetric about the crack growth direction whereas $\phi_y$contours are antisymmetric for the mode-I mother crack. Once branching occurs, however, both sets of contours become asymmetric relative to the mixed-mode daughter cracks. The first column in the figure corresponds to mode-I crack propagation of the mother crack (before branching) at time $t = 9$ μs whereas the second column represents mixed-mode crack propagation of the two daughter cracks (after branching) at time $t = 29$ μs. Again, the timestamps are with respect to crack initiation at the original notch-tip, $t = 0$. Evidently, locating the crack-tip from these DGS contours is quite obvious when compared to the displacement fields from DIC (Fig. 9) discussed earlier. This is due to the singular nature of the stress gradient fields [26] obtained from DGS. That is, the contours representing each of the measured fields have a lobed structure converging at the crack-tip, marked in Fig. 17 (and the supplementary material) by a solid white dot, making it relatively easy to locate at each time instant from any of the three fields. In this work, ϕ_r was used to locate the crack-tip and track the crack path by a series of successive white dots. That is, as can be seen from Fig. 17, once the deformation contours are plotted, the instantaneous crack-tip position becomes self-evident as the location where the contour maps form a closed lobe encircling the crack-tip in the ϕ_r field. Thus measured apparent crack length and velocity histories are shown in Figs. 18(a) and (b),

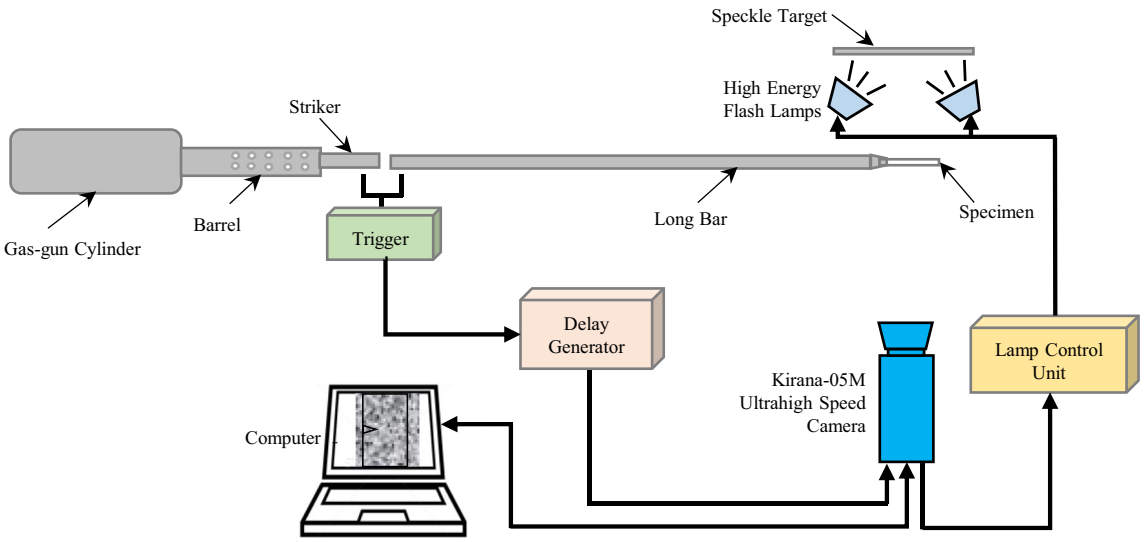

Fig. 14 Schematic of experimental setup (top-view) for DGS method to study dynamic fracture of soda-lime glass

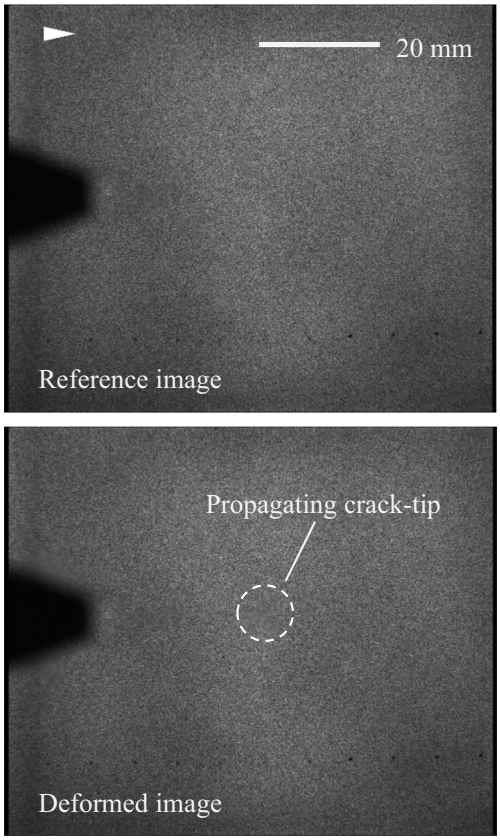

Fig. 15 Speckle images from DGS in the undeformed (top) and deformed (bottom) states for propagating crack-tip recorded by camera through the soda-lime glass specimen

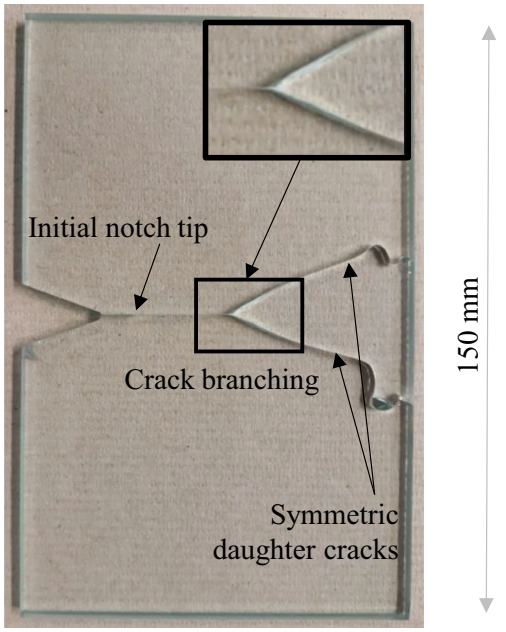

Fig. 16 Reconstructed fractured soda-lime glass specimen used in DGS experiment

respectively. The crack length increased monotonically until the end of the observation window. And, a decrement in crack length can be noted just before the crack branching phase over $t = 18$–21 μs. Subsequently, the crack length increased steadily. The crack-tip locations of the two mixed-mode daughter cracks were such that the instantaneous crack lengths were also in good agreement with each other indicating that the two daughter cracks grew symmetrically relative to the mode-I mother crack's growth direction. These observations are akin to the ones from the photoelastic experiment. Furthermore, despite the usage of speckles in DGS, the measured crack length history is relatively smooth with minimum experimental noise. Subsequently, the crack length history was processed using Bezier curves as described earlier to extract the apparent crack velocity (V) using the backward difference method. The result is shown in Fig. 18(b). The crack propagated steadily to ~1530 m/s over a ~4 μs period. Further, the crack maintained an average velocity of 1400–1550 m/s in the pre-branching phase, consistent with the one reported in [27]. As the crack entered the branching phase between $t = 18$–21 μs, the apparent crack velocity gradually reduced to values between 1250 to 1050 m/s. This is again, similar to the observation made in the photoelastic experiment. Subsequently, the crack branched into two mixed-mode daughter cracks, both of which almost instantaneously accelerated to ~1700 m/s. Subsequently, the two daughter cracks decelerated back to ~1500 m/s until the end of the observation window.

Stress Intensity Factors

Using the two orthogonal angular deflection fields in the global x, y coordinates, the instantaneous crack-tip fields in the local coordinates (x', y') (x' coinciding with the instantaneous crack growth direction) for a moving crack were obtained by performing coordinate transformation:

$$\phi_{x'} = \phi_x \cos\theta(t) + \phi_y \sin\theta(t) \tag{6}$$

The mode-I and mode-II SIFs were then evaluated by analyzing the data around the crack-tip in conjunction with the asymptotic equation [41]:

$$\phi_{x'} = C_\sigma B \left[\begin{array}{l} -\frac{1}{2} r_I^{-\frac{3}{2}} \left\{ f(V;C_L;C_S) A_1(t) \cos\left(\frac{3\theta_I}{2}\right) + g(V;C_L;C_S) D_1(t) \sin\left(-\frac{3\theta_I}{2}\right) \right\} \\ + \sum_{N=2}^{\infty} \left\{ A_N(t) \left(\frac{N}{2}-1\right) r_I^{\left(\frac{N}{2}-1\right)} \cos\left(\left(\frac{N}{2}-2\right)\theta_I\right) + D_N(t) \left(\frac{N}{2}-1\right) r_I^{\left(\frac{N}{2}-1\right)} \sin\left(\left(\frac{N}{2}-2\right)\theta_I\right) \right\} \end{array} \right] \tag{7}$$

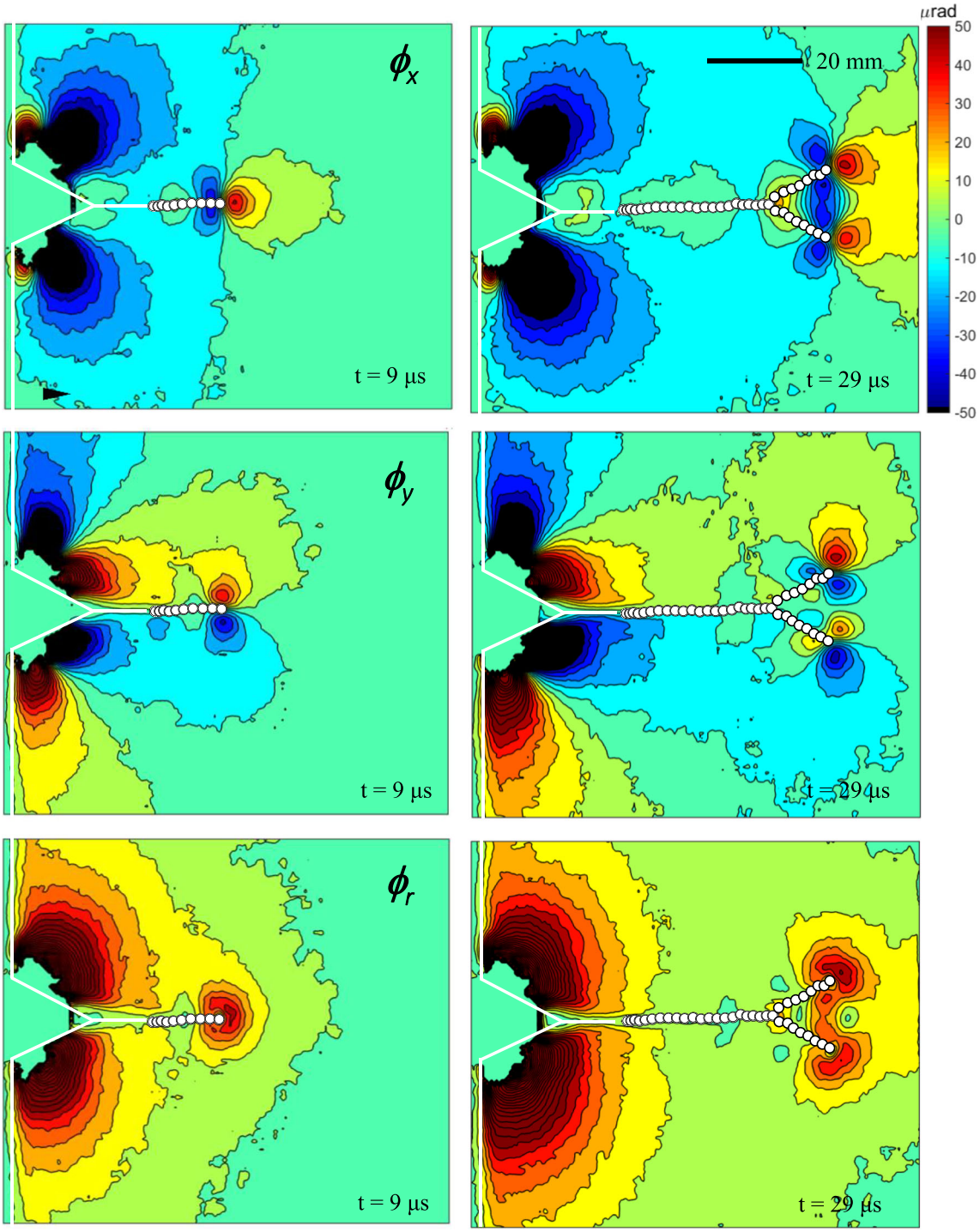

Fig. 17 Angular deflection contours in soda-lime glass subjected to dynamic loading. The arrowhead (in the top left image) shows crack growth direction. White markers indicate crack-tip locations in the previous frames. (Time, $t = 0$ corresponds to crack initiation at the original notch-tip)

using an over-deterministic least-squres approach. In the above, f and g are functions of instantaneous crack velocity V, and (r_l, θ_l) denote the local crack-tip polar coordinates obtained by contracting the local coordinates (x', y') as, $r_l = \sqrt{(x')^2 + \alpha_L^2 (y')^2}$ and $\theta_l = \tan^{-1}\left(\frac{\alpha_L y'}{x'}\right)$ in the crack growth direction. The coefficients $A_I(t)$ and $D_I(t)$ in the asymptotic series are related to the mode-I and mode-II SIFs, respectively, as $K_I^d(t) = A_1(t)\sqrt{\frac{\pi}{2}}$ and $K_{II}^d(t) = D_1(t)\sqrt{\frac{\pi}{2}}$. The functions f and g are, $f(V; C_L, C_S) = \left(\frac{1+\nu}{1-\nu}\right)\frac{\left(1+\alpha_S^2\right)\left(1-\alpha_L^2\right)}{4\alpha_S\alpha_L - \left(1+\alpha_S^2\right)^2}$ and $g(V; C_L, C_S) = \left(\frac{1+\nu}{1-\nu}\right)\frac{2\alpha_S\left(1-\alpha_L^2\right)}{4\alpha_S\alpha_L - \left(1+\alpha_S^2\right)^2}$ where $\alpha_L = \sqrt{1 - \frac{\rho(1-\nu)}{2\mu}V^2}$ and $\alpha_S =$

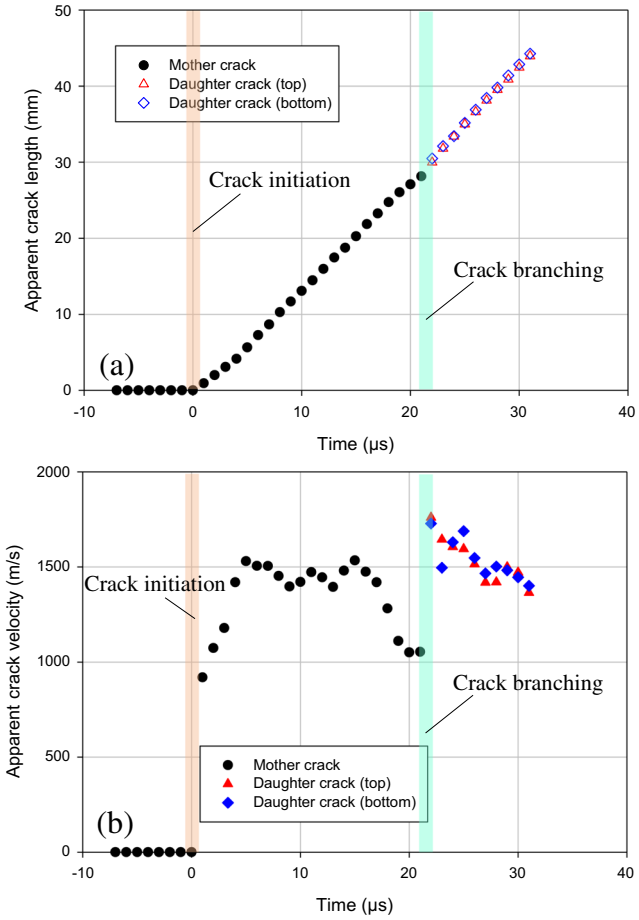

Fig. 18 Apparent crack length (top) and velocity (bottom) histories from DGS. (Time, $t = 0$ corresponds to crack initiation at the original notch-tip)

$\sqrt{1-\frac{\rho}{\mu}V^2}$ for plane stress, μ and ρ are shear modulus and mass density, respectively. For analysis purposes, the data near the crack-tip in the region $0.5 \le r/B \le 1.5$with an angular extent of $-150° \le \theta_l \le 150°$ was considered. The least-squares analysis was performed choosing four ($N = 4$) terms in the stress field. In Eq. (7), C_σ is the elasto-optic constant for SLG, and B is the initial thickness.

The SIF histories measured by DGS from crack initiation to branching are shown in Fig. 19. Here $t = 0$ corresponds to crack initiation at the original notch-tip. The mode-I SIFs increased steadily to ~0.75 MPa√m until crack initiation as shown in Fig. 19. Upon crack initiation, the SIFs dropped noticeably over ~2 μs to ~0.6 MPa√m due to unloading before increasing for the next ~8 μs to ~1.06 MPa√m rapidly. After branching, the mode-I SIF decreased quickly, followed by a steady growth for the next ~4 μs. The mode-II SIF values were relatively small when compared to the mode-I counterparts until branching occurred. (The non-zero mode-II SIF values in the pre-initiation period provide estimates of error in the least-squares data analysis.) The magnitude of the mode-II SIFs of the two daughter cracks increased immediately after the crack branching event, followed by a steady drop over the next ~4 μs. Finally, the daughter cracks continued to grow in a mixed-mode fashion with nearly constant mode-I and mode-II SIFs until the end of the observation window.

Impact Force History

The force histories imposed on the V-notch flanks of the specimen by the long-bar were also evaluated from DGS measurements by using them in conjunction with the solution for a line-load on an edge of a planar elastic solid. By assuming the functional form of the Flamant's solution [29] to hold, the normal forces acting on the specimen were expressed in terms of measured angular deflections of light rays as,

$$\phi_r = \sqrt{\phi_x^2 + \phi_y^2} = C_\sigma B \frac{2F(t)}{\pi B r^2} \tag{8}$$

where, C_σ is elasto-optic constant of SLG and B is specimen thickness. The normal force F at each time instant on the upper and lower flanks was evaluated using Eq. (6) and an over-deterministic least square-analysis for the data in the region $0.75 \le r/B \le 1.75$ where r is the radial distance from the loading point. The analysis assumed a normal contact and neglected frictional effects. Thus obtained normal forces for the upper and lower flanks and the average normal force history is shown in Fig. 20. As evident from the plots, the upper flank experienced contact forces slightly before the lower flank due to experimental asymmetry, well captured by DGS. Yet, the individual force histories show the 'ramp-up, plateau, ramp-down' pattern, similar to the one observed in the photoelastic experiment (see, Fig. 6). More importantly, the magnitudes of stresses evaluated from DGS and photoelasticity are very similar in terms of the peak force (~500 N) values even though they are two nominally identical but different experiments. The loading rate based on the average force history in the ramp-up phase is ~142 MN/s, again rather close to the value in the photoelastic experiment. These confirm that DGS measurements could be used not only to map the crack-tip fields but the impact load history as well with high fidelity.

Discussion

One analog and two digital full-field methods - photoelasticity, DIC and DGS - were implemented to visualize and quantify macroscale dynamic fracture of soda-lime glass (SLG), a rather challenging material for photomechanics investigation. The outcomes based on three nominally identical

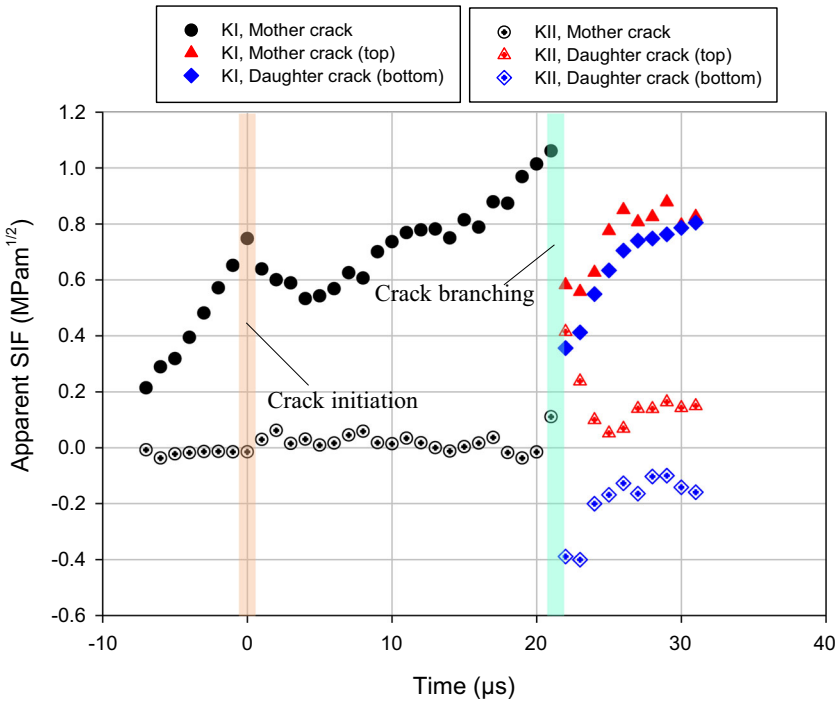

Fig. 19 Apparent stress intensity factor histories from DGS. (Time, $t = 0$ corresponds to crack initiation at the original notch-tip)

but different experiments provide new insights into the capabilities of these methods for future investigation of such low-toughness and high-stiffness glasses and ceramics. The results could also guide the selection and implementation of these methods at suitable length scales in the near term or spur enhancements to the methods in the long term. Conventional photoelasticity results show that insufficient birefringence of SLG along with its low fracture toughness precludes the method from being able to extract SIFs from crack-tip field measurements. It, however, can provide precise location of the instantaneous crack-tip as well as features corresponding to contact stresses due to Rayleigh wave propagation (stitch marks in Fig. 4) along the crack flanks with a hairline separation. The standard 2D DIC methodology is also quite limited

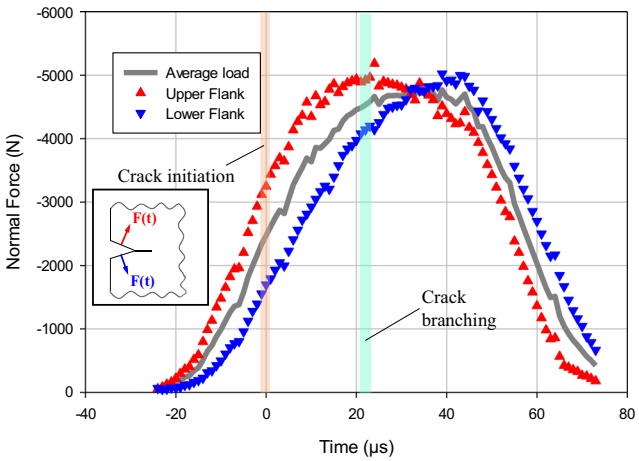

Fig. 20 Contact force history measured from DGS method

in terms of its ability to both locate the instantaneous crack-tip (directly from the non-singular deformation fields) and extract SIFs accurately using displacements evaluated close to the measurement limit during high-speed crack growth in SLG. The singular strain fields are equally ineffective since numerical differentiation of noisy displacements further exaggerate errors that exist in the measurements. The DGS methodology, on the other hand, is rather effective in studying this challenging material system since it incorporates both elasto-optic effects and signal (speckle shift) amplification using an 'optical lever.' The measured DGS quantities being proportional to the in-plane stress gradients and singular near a crack-tip, locating the instantaneous tip from the data is easier. The extracted SIFs are equally reliable in terms of magnitude as well as trend during the fracture event.

Regarding the underlying mechanics of SLG fracture, results from both photoelasticity and DGS consistently show a decreasing *apparent* crack velocity from a relatively steady value of ~1500 m/s (approx. $0.48C_R$) in the so-called mirror and mist phases of growth [2] to ~1000 m/s prior to macroscale crack branching event signaling the crack entering the hackle phase (or random *microscale* branch formations on the crack surfaces). As noted in the literature [42], hackle formations are a precursor to the ensuing crack branching event. Interestingly, despite the measured velocity trends, the *apparent* SIFs from DGS monotonically increase over the mirror to mist to hackle zones suggesting the likelihood of a critical SIF for branching to occur. Considering the monotonic increase of the *apparent* mode-I SIF from about 0.6 MPa√m after crack initiation from the initial notch-tip to ~1.1 MPa√m

prior to branching, a twofold increase of SIF as seen in previous works, is evident. Lastly, the direction of crack branches relative to the mode-I crack, however, need to be explained and will be attempted in the next phase of this ongoing research.

Conclusions

The issue of implementing full-field optical methods to study dynamic crack initiation, growth and branching events in a high-stiffness and low-toughness material such as soda-lime glass (SLG) was addressed in this paper. Three different methods - photoelasticity, 2D DIC and DGS - were all implemented for mapping mechanical fields during dynamic fracture of V-notched SLG specimens subjected to stress wave loading in three separate but nominally identical experiments. The major outcomes are summarized as follows:

- The photoelastic recordings allowed precise visualization and quantification of crack length history and reliable velocity history. The stress intensity factor histories, however, could not be evaluated due to the lack of well-formed crack-tip fringes. Hence photoelastic method is suitable to test a velocity based criteria of crack growth and branching in SLG. However, criteria pertaining SIFs and/or energy release rate cannot be verified.
- The 2D DIC approach did not allow direct visualization of the crack-tip at different time instants. The identification of the crack-tip via dominant displacement fields did not fare any better. The former being a non-singular kinematic quantity, the uncertainty in locating the crack-tip was prohibitively high. These resulted in unrealistic instantaneous velocities and stress intensity factors both in terms of trends and magnitudes. Thus it was concluded that crack velocity and stress intensity factor histories cannot be correctly quantified using DIC.
- The DGS method, though relies on principles of 2D DIC to quantify speckle shifts, measures quantities that are proportional to in-plane stress gradients in the whole field. This feature permitted visualization and quantification of crack length and crack velocity histories with high precision due to the singular nature of the resulting mechanical fields. The measured values were also in close agreement with the photoelastic counterparts. Furthermore, the dynamic fracture characteristics such as instantaneous stress intensity factors including crack initiation and growth toughness values were measured with good precision. Thus, both velocity, stress intensity factor and and/or energy release rate criteria can be readily verified using DGS.
- Finally, the profile, magnitude and duration of normal force histories acting on the V-notch flanks of the specimen measured using photoelasticity and DGS corroborated well with each other in two nominally identical but different experiments. Thus, the speckle-based digital method - DGS - fares well relative to the well-established analog photoelastic method.

Acknowledgements Partial support for this research through Army Research Office grants W911NF-16-1-0093, W911NF-15-1-0357 (DURIP) and W911NF-17-1-0355-RI are gratefully acknowledged.

References

1. Field JE (1971) Brittle fracture: its study and application. Contemp Phys 12:1–31
2. Ravi-Chandar K, Knauss WG (1984) An experimental investigation into dynamic fracture: II. Microstructural aspects. Int J Fract 26(1):65–80
3. Ravi-Chandar K, Knauss WG (1984) An experimental investigation into dynamic fracture: IV. On the interaction of stress waves with propagating cracks. Int J Fract 26(3):189–200
4. Ramulu M, Kobayashi AS (1985) Mechanics of crack curving and branching - a dynamic fracture analysis. Dynamic Fracture:61–75
5. Yoffe EH (1951) The moving Griffith crack. Philosophical Magazine and Journal of Science 42(330):739–750
6. Congleton J, Fetch NJ (1967) Crack-branching. Philos Mag 16(142):749–760
7. Sharon E, Gross SP, Fineberg J (1995) Local crack branching as a mechanism for instability in dynamic fracture. Phys Rev Lett 74(25):5096–5099
8. Xu D, Liu Z, Liu X, Zeng Q, Zhuang Z (2014) Modeling of dynamic crack branching by enhanced extended finite element method. Comput Mech 54(2):489–502
9. Bobaru F, Zhang G (2015) Why do cracks branch? A peridynamic investigation of dynamic brittle fracture. Int J Fract 196(1–2):59–98
10. Dally JW (1979) Dynamic photoelastic studies of fracture. Exp Mech 19(10):349–361
11. Bradley W, Kobayashi A (1971) Fracture dynamics—a photoelastic investigation. Eng Fract Mech 3(3):317–332
12. Ramulu M, Kobayashi A, Kang B (n.d.) Dynamic crack branching—A Photoelastic evaluation. Fifteenth Symposium, Fracture Mechanics
13. Tippur HV, Krishnaswamy S, Rosakis AJ (1991) A coherent gradient sensor for crack tip deformation measurements: analysis and experimental results. Int J Fract 48(3):193–204
14. Krishnaswamy S, Tippur HV, Rosakis AJ (1992) Measurement of transient crack-tip deformation fields using the method of coherent gradient sensing. Journal of the Mechanics and Physics of Solids 40(2):339–372
15. Tippur HV, Krishnaswamy S, Rosakis AJ (1991) Optical mapping of crack tip deformations using the methods of transmission and reflection coherent gradient sensing: a study of crack tip K-dominance. Int J Fract 52(2):91–117
16. Conner R, Rosakis A, Johnson W, Owen D (1997) Fracture toughness determination for a beryllium-bearing bulk metallic glass. Scr Mater 37(9):1373–1378
17. Kirugulige MS, Tippur HV (2009) Measurement of fracture parameters for a mixed-mode crack driven by stress waves using image correlation technique and high-speed digital photography. Strain 45(2):108–122
18. Lee D, Tippur H, Kirugulige M, Bogert P (2009) Experimental study of dynamic crack growth in unidirectional graphite/epoxy

composites using digital image correlation method and high-speed photography. J Compos Mater 43(19):2081–2108
19. Feiteira J, Tsangouri E, Gruyaert E, Lors C, Louis G, Belie ND (2017) Monitoring crack movement in polymer-based self-healing concrete through digital image correlation, acoustic emission analysis and SEM in-situ loading. Mater Des 115:238–246
20. Makki EA, Parrikar PN, Shukla A (2015) Response of coated laminated glass panels subjected to combined blast and temperature loadings. Journal of Dynamic Behavior of Materials 1(4):409–422
21. Reu PL, Rogillio BR, Wellman GW (2007) Crack tip growth measurement using digital image correlation. Experimental Analysis of Nano and Engineering Materials and Structures:555–556
22. Periasamy C, Tippur HV (2012) Full-field digital gradient sensing method for evaluating stress gradients in transparent solids. Appl Opt 51(12):2088
23. Periasamy C, Tippur HV (2012) Measurement of orthogonal stress gradients due to impact load on a transparent sheet using digital gradient sensing method. Exp Mech 53(1):97–111
24. Sundaram BM, Tippur HV (2016) Dynamics of crack penetration vs. branching at a weak interface: an experimental study. Journal of the Mechanics and Physics of Solids 96:312–332
25. Sundaram, B. M., and Tippur, H. V. (2018). Dynamic crack branching in soda-lime glass: an optical investigation using digital gradient sensing. Dynamic behavior of materials, volume 1 conference proceedings of the Society for Experimental Mechanics Series, 51-56
26. Sundaram BM, Tippur HV (2017) Full-field measurement of contact-point and crack-tip deformations in soda-lime glass. Part-II: stress wave loading. Int J Appl Glas Sci 9(1):123–136
27. Sundaram BM, Tippur HV (2018) Dynamic fracture of soda-lime glass: A full-field optical investigation of crack initiation, propagation and branching. Journal of the Mechanics and Physics of Solids 120:132–153
28. Prautzsch H, Boehm W, Paluszny M (2011) Bezier and B-spline techniques. Springer, Berlin
29. Budynas RG (1999) Advanced strength and applied stress analysis. WCB/McGraw-Hill, Boston
30. Chao YJ, Luo PF, Kalthoff JF (1998) An experimental study of the deformation fields around a propagating crack tip. Exp Mech 38(2): 79–85
31. Kirugulige MS, Tippur HV, Denney TS (2007) Measurement of transient deformations using digital image correlation method and high-speed photography: application to dynamic fracture. Appl Opt 46(22):5083
32. Abanto-Bueno J, Lambros J (2002) Investigation of crack growth in functionally graded materials using digital image correlation. Eng Fract Mech 69(14–16):1695–1711
33. Lopez-Crespo P, Shterenlikht A, Patterson EA, Yates JR, Withers PJ (2008) The stress intensity of mixed mode cracks determined by digital image correlation. The Journal of Strain Analysis for Engineering Design 43(8):769–780
34. Yoneyama S, Morimoto Y, Takashi M (2006) Automatic evaluation of mixed-mode stress intensity factors utilizing digital image correlation. Strain 42(1):21–29
35. Mathieu F, Hild F, Roux S (2012) Identification of a crack propagation law by digital image correlation. Int J Fatigue 36(1):146–154
36. Peters WH, Ranson WF (1982) Digital imaging techniques in experimental stress analysis. Opt Eng 21(3)
37. Rubino V, Rosakis AJ, Lapusta N (2017) Understanding dynamic friction through spontaneously evolving laboratory earthquakes. Nat Commun 8(1)
38. Yoneyama S, Ogawa T, Kobayashi Y (2007) Evaluating mixed-mode stress intensity factors from full-field displacement fields obtained by optical methods. Eng Fract Mech 74(9):1399–1412
39. Jin H, Bruck H (2005) Pointwise digital image correlation using genetic algorithms. Exp Tech 29(1):36–39
40. Poissant J, Barthelat F (2009) A novel "subset splitting" procedure for digital image correlation on discontinuous displacement fields. Exp Mech 50(3):353–364
41. Sundaram B, Tippur H (2015) Dynamic crack growth Normal to an Interface in bi-layered materials: an experimental study using digital gradient sensing technique. Exp Mech 56(1):37–57
42. Rose LRF (1976) Recent theoretical and experimental results on fast brittle fracture. Int J Fract 12(6):799–813